

Hydrogen Spillover-Driven Low Temperature Synthesis of High-Entropy Alloy Nanoparticles as a Robust Catalyst

Kohsuke Mori

Osaka University <https://orcid.org/0000-0003-3915-4528>

Naoki Hashimoto

Osaka University

Naoto Kamiuchi

The Institute of Scientific and Industrial Research, Osaka University <https://orcid.org/0000-0002-4145-5226>

Hideto Yoshida

Osaka University

Hisayoshi Kobayashi

Kyoto Institute of Technology

Hiroshi Yamashita (✉ yamashita@mat.eng.osaka-u.ac.jp)

Osaka University

Article

Keywords: High-entropy alloys, nanoparticles, catalysts

Posted Date: March 19th, 2021

DOI: <https://doi.org/10.21203/rs.3.rs-322594/v1>

License:   This work is licensed under a Creative Commons Attribution 4.0 International License.

[Read Full License](#)

Version of Record: A version of this preprint was published at Nature Communications on June 23rd, 2021. See the published version at <https://doi.org/10.1038/s41467-021-24228-z>.

Abstract

High-entropy alloys (HEAs) have been intensively pursued as potentially advanced materials because of their exceptional properties. However, the facile fabrication of nanometer-sized HEAs over conventional catalyst supports remains challenging, and the design of rational synthetic protocols would permit the development of innovative catalysts with a wide range of potential compositions. Herein, we demonstrate that titanium dioxide (TiO_2) is a promising platform for the low-temperature synthesis of supported CoNiCuRuPd HEA nanoparticles (NPs) at 400°C . This process is driven by the pronounced hydrogen spillover effect on TiO_2 in conjunction with coupled proton/electron transfer. In this process, Pd nuclei generated in the early stage act as uptake sites to enhance the migration of active hydrogen atoms, and the five component metals are simultaneously reduced by spilled hydrogen on the support rather than via direct reduction by gaseous H_2 . The CoNiCuRuPd HEA NPs on TiO_2 produced in this work were found to be both active and extremely durable during the CO_2 hydrogenation reaction. Characterization by means of various *in situ* techniques and theoretical calculations elucidated the specific mechanism by which the HEA NPs were formed and also established that a synergistic effect was obtained from this combination of elements.

Introduction

In contrast to conventional alloy materials based on single principal elements, high-entropy alloys (HEAs) have recently received significant attention in various research fields. These alloys represent a new class of metallic materials in which more than five near-equimolar components are mixed to form single-phase solid solutions with high mixing entropy values, rather than intermetallic phases.^{1,2} Various unique synergistic effects result from such mixtures, including high configuration entropy, lattice distortion, sluggish diffusion and cocktail effects, and endow HEAs with high mechanical strength, good thermal stability and superior corrosion resistance.³⁻⁵ To date, several synthetic strategies have been reported, such as bulk melting,⁶ solid state processing⁷ and additive manufacturing,^{8,9} all of which have principally focused on the fabrication of bulk HEAs. However, the development of HEA nanoparticles (NPs) with a mean diameter of less than 10 nm lags significantly behind, despite the potential practical applications of these NPs in catalysis, nanoelectronics and material science owing to their large surface area-to-volume ratio and nanoscale size effect.¹⁰

A bottom-up approach to the fabrication of HEA NPs is likely to be more reliable than a top-down approach, because the former would be expected to produce fewer surface defects along with uniform chemical compositions and homogenous size distributions.¹¹ In an early study, Yao et al. succeeded in the fabrication of HEA NPs containing up to eight elements on conductive carbon nanofibers, using a carbothermal shock method based on flash heating (at approximately 10^5 K/s) to approximately 2000 K followed by rapid cooling (at the same approximate rate).¹²⁻¹⁴ Subsequently, methods incorporating ultrasonication,¹⁵ solvothermal synthesis,¹⁶ polyols in solution^{17,18} and fast moving bed pyrolysis¹⁹ were explored as alternative synthetic approaches. Unfortunately, these methods still require the application of

high temperatures and special experimental apparatuses. The development of new and simpler techniques for the synthesis of HEA NPs, especially those immobilized on the surfaces of conventional support materials, represents an ongoing challenge. Even so, such research could result in a wider range of industrial uses for these materials and provide a better understanding of the novel functions of nanostructured catalysts.

Hydrogen spillover is a fascinating phenomenon that occurs in sensors, hydrogen storage materials and heterogeneous catalysis.²⁰⁻²² This process involves the surface migration of dissociated H atoms driven by a concentration gradient. Hydrogen spillover on reducible transition metal oxides such as TiO₂, WO₃ and MoO₃ proceeds via a set sequence of steps. These are: (i) the dissociative chemisorption of H₂ upon interacting with a noble metal, (ii) the formation of protons (H⁺) and electrons (e⁻) from H atoms at metal-support interfaces and (iii) the diffusion of these protons to lattice O₂⁻ anions to form O-H and H-O-H bonds, accompanied by the simultaneous partial reduction of the metals in the transition metal oxide by the electrons.^{23,24} Thus, in this process, H atoms migrate to adjacent hydrogen-poor metal oxide surfaces, which would not be able to dissociate H₂ molecules under the same conditions, via coupled proton/electron transfer. Consequently, the extent of hydrogen spillover on non-reducible supports is limited because the simultaneous transfer of protons and electrons will not proceed on such materials.²⁵ Recently, van Bokhoven et al. reported experimental data in conjunction with theoretical calculations showing that hydrogen spillover on TiO₂ proceeds ten orders of magnitude faster than on the non-reducible oxide Al₂O₃, and that TiO₂ provides longer migration distances from the noble metal proton sources.²⁶

Our own group has previously demonstrated that TiO₂ is a promising platform for the synthesis of non-equilibrium binary alloy NPs, such as RuNi and RhCu, which are essentially immiscible at equilibrium due to the positive enthalpies of formation of their solid solution alloys.^{27,28} However, the highly specific formation of binary alloy NPs based on combinations of normally immiscible noble and base metals can be achieved with the assistance of the strong spillover effect obtained from TiO₂. Using this oxide allows spillover hydrogen species with high reduction potentials to be generated from noble metals (Ru or Rh) and to rapidly migrate to and reduce base metals (Ni or Cu) at low temperatures. In the present work, we developed and demonstrated that this facile strategy can be applied to the synthesis of TiO₂-supported HEA NPs. Specifically, CoNiCuRuPd HEA NPs on TiO₂ displayed high activity and outstanding stability during the CO₂ hydrogenation reaction. This study also elucidated the specific mechanism responsible for the formation of HEA NPs, based on *in situ* characterization techniques. In addition, density functional theory (DFT) calculations were performed to validate both the formation mechanism and to examine the synergistic effects of mixing multiple elements, such as unique catalytic performance and exceptional durability.

Results

Synthesis and characterization of HEA NPs on TiO₂

CoNiCuRuPd HEA NPs supported on TiO₂ (CoNiCuRuPd/TiO₂) were synthesized using a simple impregnation method, employing an aqueous solution of the corresponding precursors. This was followed by reduction under a H₂ atmosphere at 400 °C without a specific calcination step before this reduction. A survey of bulk multi-component alloys determined that the formation of a solid solution HEA required an atomic size difference, δ , of less than 6.6% and an enthalpy of mixing, DH_{mix} , between -11.6 and 3.2 kJ/mol.²⁹ In the present study, the CoNiCuRuPd combination met the above criteria ($\delta = 3.9\%$ and $DH_{\text{mix}} = 1.1$ kJ/mol), and so the formation of solid solution CoNiCuRuPd HEA NPs was expected.

Figure 1A shows the H₂ temperature programmed reduction (TPR) profiles obtained from the as-deposited mono- and quinary-component samples prior to reduction under H₂. These data indicate that the single metals generated broad reduction peaks at different temperatures. In addition, the absence of a peak in the case of the Pd/TiO₂ sample suggests the immediate reduction of the deposited Pd²⁺ precursor after the switching between H₂ and Ar flows at ambient temperature.³⁰ The relative trend in the reduction temperatures of these materials is similar to that of the reduction potentials of the respective ions ($E^0(\text{Co}^{2+}/\text{Co}^0) = -0.28$ V, $E^0(\text{Ni}^{2+}/\text{Ni}^0) = -0.26$ V, $E^0(\text{Cu}^{2+}/\text{Cu}^0) = +0.34$ V, $E^0(\text{Ru}^{3+}/\text{Ru}^0) = +0.46$ V and $E^0(\text{Pd}^{2+}/\text{Pd}^0) = +0.99$ V, all vs. NHE). Interestingly, the quinary-component precursors on TiO₂ generated only a single reduction peak with a maximum temperature of approximately 170 °C, which was intermediate between those obtained from the mono-component samples. Thus, the reducibility of each of the Co²⁺, Ni²⁺ and Cu²⁺ ions was improved while those of the Ru²⁺ and Pd²⁺ ions were decreased in comparison with the monometallic samples. This simultaneous reduction of the mixed-metal precursors indicates that all atoms were undergoing interactions with one another, leading to the formation of HEA NPs containing all five elements. In contrast, the quinary-component precursors on the non-reducible supports such as MgO and Al₂O₃ displayed broad reduction peaks ranging from 130 to 250 °C. These reduction profiles indicated that all atoms were not interacting on the MgO and Al₂O₃ surfaces.

In situ X-ray absorption fine structure (XAFS) analyses conducted under a H₂ atmosphere at elevated temperatures further elucidated the reduction sequence (**Figures S1, S2 and 1B**). X-ray absorption near-edge structure (XANES) spectra confirmed the reduction of all the precursors at 200 °C. The intermediate shapes and edge positions at the Co and Ni K-edges indicated the presence of a mixture of cations and zero valent ions at 200 °C, due to their relatively low reduction potentials. In contrast, all spectra acquired at 400 °C resembled those of the corresponding foils, suggesting that all the elements were in a metallic state. More detailed inspection of these data also found slight changes in the post-edge region at all K-edges. As an example, the two distinct peaks at approximately 24,390 and 24,415 eV corresponding to the allowed 1s → 5p transition at the Pd K-edge were slightly shifted to higher energy values compared to the Pd foil. This result suggested that the symmetry of the Pd metal face centered cubic (*fcc*) structure was slightly disordered following integration with the other metals.³¹

Fourier transforms of extended X-ray absorption fine structure (FT-EXAFS) data further clarified the structural transformation during the reduction sequence. The spectra of the as-deposited sample produced a sharp singlet peak in the K-edge region that was attributed to M–O bonds with lengths of approximately 1.7–1.9 Å. In the case of Co and Ni, the peak intensity due to the M–O bonds decreased at 200 °C, whereas another peak attributed to metallic M–M bonds with longer interatomic distances appeared for Cu, Ru and Pd. These transitions demonstrated the reduction of Mⁿ⁺ ions on the TiO₂ support. The bond structure after completion of the reduction revealed that the interatomic metallic M–M bond lengths were significantly different from those for the corresponding bulk references, suggesting that those elements were surrounded by different metallic atoms.

The X-ray diffraction (XRD) pattern for CoNiCuRuPd/TiO₂ exhibited new broad peaks at $2\theta = 42.2^\circ$ and 48.9° . These peaks suggest the formation of a single phase with an *fcc* structure having a lattice parameter (*a*) of 3.734 Å, which is intermediate between 3.890 Å (for *fcc* Pd) and 3.524 Å (for *fcc* Ni) (**Figure 2A**). No peaks attributable to pure Co, Ni, Cu, Ru or Pd were detected, establishing that these components were homogeneously dispersed in the NPs without segregation. **Figures 2B** and **C** present high-angle annular dark field scanning TEM (HAADF-STEM) images showing a lattice fringe spacing of 2.18 Å. From these images, the average size (d_{ave}) of the CoNiCuRuPd HEA NPs was estimated to be 1.90 nm (**Figure 2C**). The energy dispersive X-ray (EDX) maps of these specimens also confirmed the homogeneous distribution of each element (**Figures 2D-H**). In addition, an EDX line analysis showed that all signals appeared in the same area, demonstrating the formation of a solid solution alloy involving all five elements (**Figure S3**). The d_{ave} values for the CoNiCuRuPd/Al₂O₃ and CoNiCuRuPd/MgO samples were 6.65 nm and 6.73 nm, respectively, (**Figure S4**) and partially segregated NPs with a bimodal particle size distribution were observed on the MgO support. These results suggest that the TiO₂ support ensured more rapid and homogeneous reduction at lower temperatures, allowing the formation of nuclei to provide smaller, uniform HEA NPs without segregation.

Formation mechanism driven by hydrogen spillover over TiO₂

Considering the H₂-TPR and *in situ* XAFS results, we propose a mechanism for the formation of the HEA NPs on the TiO₂ support in conjunction with hydrogen spillover (**Figure 3A**). In this process, under a H₂ atmosphere, the Pd²⁺ precursors are first partially reduced to generate nuclei that appear to be stabilized at defect sites on the TiO₂. Following this, H₂ is dissociated on the surfaces of these Pd nuclei to form Pd–H species (**Step 1**). The reduction of Ti⁴⁺ to Ti³⁺ together with the transfer of H atoms from Pd nuclei at the metal-support interfaces (**Step 2**) is accompanied by the migration of electrons from Ti³⁺ ions to neighbouring Ti⁴⁺ ions. This promotes the subsequent simultaneous transfer of protons to O²⁻ anions attached to these adjacent Ti⁴⁺ ions (**Step 3**). In this manner, the hydrogen atoms rapidly reach all metal ions by moving over the TiO₂ surface (**Step 4**), such that these ions are all reduced at the same time to form the HEA NPs.

This mechanism based on the spillover effect was further evaluated by DFT calculations, using rutile TiO_2 (101) as a model because of its thermodynamic stability and Pd_5 clusters as a model for Pd nuclei. According to the above proposed reaction mechanism, four representative elementary steps were considered for the reduction of metal cations on the TiO_2 through the hydrogen spillover from Pd clusters. The resulting potential energy profile is shown in **Figure 3B**. Moving along this profile, the dissociation of H_2 on a Pd_5 cluster (**Step 1**) occurs with a barrier of 20.1 kcal/mol. The activation energy (E_a) associated with subsequent H atom transfer from a Pd_5 cluster to a neighbouring O atom on the support (**Step 2**) was estimated to be 27.5 kcal/mol. Owing to the presence of oxygen sites having different coordination numbers, such as 2-coordinated oxygen (O(2)) or 3-coordinated oxygen (O(3)) sites, the migration of a H atom over the TiO_2 surface (**Step 3**) was calculated separately for each scenario. The activation energies for the migration of a H atom from O(2) to O(2), O(2) to O(3) and O(3) to O(2) sites were determined to be 15.0, 37.4 and 12.7 kcal/mol, respectively (**Figure S5**). These data demonstrate that the participation of O(3) sites in the migration of H atoms over the TiO_2 (101) is energetically unfavourable, and so this migration preferentially occurs at O(2) sites because of the abundance of such sites on TiO_2 (101). The reduction of other deposited metal cations by the spilled H atoms (**Step 4**) was further evaluated by calculating E_a for the attack of a neighbouring H atom on an $\text{M}^{n+}\text{-OH}$ species ($\text{M}=\text{Co}^{2+}$, Ni^{2+} , Cu^{2+} , Ru^{3+} or Pd^{2+}) on the support, together with the loss of H_2O . These E_a values were estimated to be 12.7, 12.7, 12.6, 8.0 and 7.4 kcal/mol for Co^{2+} , Ni^{2+} , Cu^{2+} , Ru^{3+} and Pd^{2+} , respectively. Thus, this step had the lowest energy requirement for all cations in the overall reaction.

The dissociation energy of a gaseous H_2 molecule on TiO_2 (101) without Pd clusters was estimated to be 82.3 kcal/mol (**Figure S6**). It was also calculated that the direct reduction of Co^{2+} on TiO_2 (101) by a gaseous H_2 molecule occurred with a barrier of 85.3 kcal/mol (**Figure S7**), which was more than six times greater than that for the same process with a spilled H atom. This preliminary analysis further confirmed that spilled H atoms in the presence of Pd clusters promoted the rapid and simultaneous reduction of the multiple metal precursors at low temperatures on a thermodynamic basis. In comparison, **Step 3** on hexagonal Al_2O_3 (100) was found to be thermodynamically unfavorable, with E_a values of 29.3, 41.7 and 43.8 kcal/mol for the transfer pathways from O(2) to O(3), O(3) to O(2) and O(3) to O(3) sites, respectively (**Figure S8**), which were more than twice as great as those for TiO_2 (101). Similar calculations were also performed using the $\gamma\text{-Al}_2\text{O}_3$ model proposed by Digne et al., who reported an E_a for hydrogen migration (38.9 kcal/mol) that was similar to our result for hexagonal Al_2O_3 .^{32,33} These results clearly suggest that H atom transfer on TiO_2 was energetically more likely to proceed than that on Al_2O_3 , hence the rate of hydrogen spillover was faster on the TiO_2 .

Catalytic CO_2 hydrogenation

The hydrogenation of CO₂ to high calorific fuels has the potential to alleviate both climate change and future demands for fossil fuels.^{34,35} As an example, the endothermic reverse water-gas shift reaction (CO₂ + H₂ → CO + H₂O, $DH = 41 \text{ kJ mol}^{-1}$) is one of the most promising means of producing CO as an important feedstock for Fischer-Tropsch processes and as an intermediary step for the further synthesis of fuel and chemicals.^{36,37} In addition, the exothermic CO₂ methanation reaction (CO₂ + 4H₂ → CH₄ + 2H₂O, $DH = -165.0 \text{ kJ mol}^{-1}$), also known as the Sabatier reaction, has attracted new interest because of the recent development of the power-to-gas concept.^{38,39} This reaction is also recognized as an important approach to powering long-term space exploration missions.⁴⁰

In the present work, catalytic performance was evaluated based on monitoring the progress of atmospheric pressure CO₂ hydrogenation at temperatures from 300 to 400 °C, with CO and CH₄ as the major products (**Figure 4A**). CoNiCuRuPd/TiO₂ gave the highest yield of hydrogenated products, which was from 2 and 13 times greater, respectively, than those obtained using MgO and Al₂O₃ as supports. This enhanced activity can presumably be ascribed to the formation of a quinary-component HEA NPs solely on the TiO₂, as indicated by the H₂-TPR data. Specifically, the quinary-component precursors on the MgO and Al₂O₃ displayed broad reduction peaks ranging from 130 to 250 °C, suggesting the formation of larger segregated NPs rather than smaller HEA NPs. The selectivities for CO and CH₄ were also found to vary depending on the catalyst that was employed. CoNiCuRuPd/TiO₂ showed relatively high selectivity for CH₄ (68.3% CH₄ selectivity at 400 °C), similar to that of the Al₂O₃ specimen (72.1% CH₄ selectivity at 400 °C) but quite different from that obtained using MgO (75.2% CO selectivity at 400 °C). It should also be noted that the catalytic activity of Pd/TiO₂ prepared by the same method was low compared with that of CoNiCuRuPd/TiO₂, and that this monometallic sample gave CO as the primary product. As shown in **Figure 4B**, an apparent activation energy (E_a) of 37.7 kJ/mol was obtained for CoNiCuRuPd/TiO₂, which was lower than that of 44.2 kJ/mol for Pd/TiO₂. These results clearly suggest the so-called cocktail effect originating from the synergistic effect obtained from the combination of elements comprising the HEA.

At atmospheric pressure, the most widely accepted mechanism for CO₂ hydrogenation is initiated by the adsorption and activation of CO₂ at the metal/oxide interfaces of the metal-supported catalyst.^{41,42} Hydrogenation and/or dissociation subsequently occur to afford a chemically adsorbed CO intermediate that is either desorbed as a product or undergoes further hydrogenation to form CH₄. Previous studies have demonstrated that both catalytic activity and selectivity are affected by the particle size of the active metal centres and by the metal/support interfaces.⁴³ Because the particles sizes in CoNiCuRuPd/TiO₂ ($d_{\text{ave}} = 1.90 \text{ nm}$) and Pd/TiO₂ ($d_{\text{ave}} = 2.04 \text{ nm}$) were similar (**Figure S9**), the different selectivities for CO or CH₄ observed in this study were primarily attributed to the desorption characteristics of CO molecules at metal sites with different binding strengths.

For this reason, the surfaces of the NPs were assessed using temperature programmed desorption (TPD) with adsorbed CO, together with Fourier transform infrared spectroscopy (FTIR). In the case of Pd/TiO₂, a peak assignable to the linear stretching vibration of adsorbed CO (ν_{CO}) was observed at 2091 cm⁻¹ in association with the initiation of CO desorption at 50 °C (**Figure 5A**). In contrast, this ν_{CO} peak was observed at 2070 cm⁻¹ in the spectrum obtained from CoNiCuRuPd/TiO₂. This shift toward a lower wavenumber occurred together with a change in the CO desorption temperature to above 150 °C (**Figure 5B**). These results readily explain the selectivity observed during CO₂ hydrogenation over these materials. The adsorption sites on CoNiCuRuPd/TiO₂ were definitely electron enriched compared with those on the monometallic Pd/TiO₂. This, in turn, delayed the desorption of the CO intermediate owing to the stronger interactions, thus promoting subsequent hydrogenation to form CH₄.⁴² These experimental results were also supported by theoretical DFT calculations. The frequency of CO adsorbed on *fcc* CoNiCuRuPd was modeled using randomly populated (111) facets of periodically repeating slab models (with the 15 configuration patterns depicted in **Figure S10**),⁴⁴ giving an average ν_{CO} of 2079 cm⁻¹. The adsorption energies (E_{ad}) of CO and H on an *fcc* surface, *fcc* hollow and hexagonal close packed (*hcp*) hollow were also calculated for CoNiCuRuPd(111) and for pure metal slabs (**Figure S11**). The average E_{a} values for CO and H adsorption on CoNiCuRuPd HEA (denoted as HEA_{ave}(111) in **Figure 5C**) were determined to be -37.5 and -50.3 kcal/mol, respectively. The average E_{a} for CO adsorption on Pd(111) was substantially lower at -26.2 kcal/mol, while the E_{a} for H (-54.2 kcal/mol) was similar. These results demonstrate that the interaction between CO and the HEA surface was stronger than that with the Pd surface, suggesting that CH₄ and CO would be preferentially formed on the former and latter, respectively. It should be further noted that the average E_{a} for CO and H adsorption on all the pure metals (denoted as Ave_{CoNiCuRuPd} in **Figure 5C**) was different from the HEA_{ave}(111). This result provided additional evidence for a cocktail effect originating from the synergistic effect of the combined metals, which gives rise to unique electronic properties.

Structural Robustness of HEA NPs

Another crucial phenomenon associated with HEA NPs that affects catalytic performance is the sluggish diffusion effect, which enhances the durability of the catalyst. In trials with Pd/TiO₂, the catalytic activity during CO₂ hydrogenation was found to gradually decrease with continued use, such that the relative activity was reduced by a factor of 0.76 after a 72 h reaction (**Figure 4C**). In contrast, CoNiCuRuPd/TiO₂ retained 96% of its original activity, while keeping constant selectivity. Each of these catalyst specimens was recovered after 72 h and subjected to a TEM analysis (**Figure S12**). A substantial enlargement of the NPs was observed in the case of Pd/TiO₂, such that the average NP diameter was more than doubled to 5.3 nm from 2.0 nm. Conversely, CoNiCuRuPd/TiO₂ exhibited suppressed particle growth and the mean particle diameter was determined to be 2.3 nm (**Figure S13**). The homogenous elemental distribution

evident in the EDX mapping data also provided strong evidence for the maintenance of the random HEA structure. In addition, EDX line scans confirmed that single NPs contained all the constituent elements.

The structural robustness of the HEA NPs was also confirmed by monitoring radiation damage process using TEM under electron beam irradiation in vacuum.^{45,46} Here, the contrast of atomic positions was analysed in the continuous image. As shown in the time-lapsed TEM images, the change of the contrast in the atomic column position is relatively small for the CoNiCuRuPd/TiO₂ even at edge/corner position (**Figure 6A-C**), indicating the suppression of structure deterioration by an incident electron beam. Conversely, drastic changes in contrast were observed for Pd/TiO₂, which is definitely originated from the atomic displacement induced by the knock-on damage (**Figure 6E,F**).^{47,48} The temporal changes in intensity of atomic columns at other positions showed similar trend, as summarized in **Figure S14**. The statistic and precise analysis is indispensable for discussing the number of atoms at an atomic column from the contrast of a TEM image.^{49,50} Nevertheless, the stability of the surface atoms in the CoNiCuRuPd NPs has a clear difference from the monometallic Pd NPs.

In an effort to better understand the high robustness of the HEA NPs, theoretical investigations were conducted employing cluster models. DFT calculations demonstrated that the cohesive energy (E_c) of a Co₁₆Ni₁₅Cu₁₆Ru₁₆Pd₁₆ HEA cluster was -3.92 eV, which was higher than the value of -3.09 eV for a Pd₇₉ cluster (**Figure 7A**). Combining these data with molecular dynamics (MD) simulations, diffusion coefficients (D) were determined at 900 K after 0.1 ps (**Figure S15**). The results demonstrated that the D values of all metals in a Co₁₆Ni₁₅Cu₁₆Ru₁₆Pd₁₆ HEA cluster were lower than those for the corresponding monometallic clusters (Co₇₉, Cu₇₉, Ni₇₉, Ru₇₉ or Pd₇₉) (**Figure 7B**). As an example, the D for Pd in a Co₁₆Ni₁₆Cu₁₅Ru₁₆Pd₁₆ HEA cluster was calculated to be 1.31×10^{-5} m²/s, and so was approximately one third lower than the value of 3.43×10^{-5} m²/s for a Pd₇₉ cluster. These results provide further evidence that sluggish diffusion in the HEA NPs, originating from the mixing of multiple elements as well as from lattice distortion effects, contributed significantly to the high resistance of the HEA NPs against the undesired irreversible agglomeration and radiation damage process.

Discussion

We succeeded in the facile low-temperature synthesis of supported HEA NPs, taking advantage of the hydrogen spillover that proceeds on TiO₂ via a coupled proton–electron transfer mechanism. Both *in situ* observations and theoretical simulations provided evidence that Pd²⁺ ions are first reduced by H₂ to generate nuclei, after which the dissociation of hydrogen molecules occurs to form active hydrogen atoms that enable the simultaneously reduction of neighboring precursors. A CoNiCuRuPd/TiO₂ catalyst synthesized in this manner exhibited different selectivity and significantly improved stability compared with Pd/TiO₂ during the hydrogenation of CO₂. Theoretical investigations also emphasized that the sluggish diffusion in these CoNiCuRuPd HEA NPs is caused by the combination of multiple metals, and that lattice distortion plays a crucial role in the superior robustness of this material. This study

demonstrates not only an ideal heterogeneous catalyst based on HEA NPs with durability that suggests potential practical applications, but also offers advanced insights into an innovative catalyst/photocatalyst architecture providing an essentially unlimited compositional space.

Methods

Materials

Rutile TiO₂ (JRC-TIO-6) was supplied by the Catalysis Society of Japan. Al₂O₃ was obtained from Stream Chemicals, Inc., while MgO was purchased from Wako Pure Chemical Industries, Ltd. RuCl₃·*n*H₂O, Cu(NO₃)₂·3H₂O, Co(NO₃)₂·6H₂O and Ni(NO₃)₂·6H₂O were purchased from Nacalai Tesque and Na₂PdCl₄ was obtained from the Tokyo Chemical Industry Co., Ltd. All commercially available compounds were used as received.

Preparation of catalysts

TiO₂ (0.5 g) was dispersed in distilled water (100 mL) followed by the addition of 10 mM of each metal precursor solution (4.75 mL). This mixture was stirred at room temperature for 1 h, after which the water was evaporated under vacuum. Finally, the sample was reduced under a 20 mL/min flow of H₂ at 400 °C for 2 h to yield CoNiCuRuPd/TiO₂ (Pd 1.0 wt%; Co:Ni:Cu:Ru:Pd = 1:1:1:1:1 [on a molar basis]). CoNiCuRuPd/Al₂O₃ (Pd 1.0 wt%; Co:Ni:Cu:Ru:Pd = 1:1:1:1:1), CoNiCuRuPd/MgO (Pd 1.0 wt%; Co:Ni:Cu:Ru:Pd = 1:1:1:1:1) and Pd/TiO₂ (Pd 1.0 wt.%) with the same metal loadings were also synthesized according to the same procedure.

Characterization

Transmission electron microscopy (TEM) micrographs were obtained with a field emission (FE) TEM instrument (Hf-2000, Hitachi) equipped with an energy-dispersive X-ray (EDX) detector (Kevex) operated at 200 kV. Scanning transmission electron microscopy (STEM) images, elemental mapping and line analysis were obtained using a JEOL-ARM 200F instrument equipped with a Kevex EDX detector (JED 2300T) operated at 200 kV. Temperature programmed reduction with H₂ (H₂-TPR) was conducted using a BEL-CAT (BEL Japan, Inc.) instrument by heating 50 mg samples at 5 °C/min from 50 to 600 °C under a 5.0% H₂/Ar flow. These analyses were performed using as-deposited samples before H₂ reduction. A temperature-programmed desorption (TPD) study using adsorbed CO was performed with a JASCO FT/IR-6600 instrument. In addition, *in situ* X-ray absorption fine structure (XAFS) spectra and X-ray diffraction (XRD) patterns were acquired at the 01B1 beamline station in conjunction with a Si (111) monochromator at SPring-8, JASRI, Harima, Japan (proposal numbers 2019A1048 and 2019B1091). In a typical experiment, spectra were acquired while a pellet sample was held in a batch-type *in situ* XAFS cell. XAFS data were processed using the REX2000 software program (Rigaku).

Computational method

Adsorption energies, E_{ad} , were calculated using the density functional theory (DFT), employing DMol³ program^{51,52} with Materials Studio 17.2 interface. The generalized gradient approximation (GGA) exchange-correlation functional proposed by Perdew, Burke and Ernzerhof (PBE)⁵³ was combined with the double numerical plus polarization (DNP) basis sets. A slab consisting of a 4×4 surface unit cell was adopted. The slab consists of three atomic (111) layers. The geometry of bottom two layers was fixed at the corresponding bulk positions, and that of top layer and adsorbate was allowed to relax during geometry optimizations. The lattice constant to the surface normal direction was taken to 30 \AA including the vacuum region. E_{ad} was defined by the equation $E_{\text{ad}} = E_{\text{adsorbate/slab}} - (E_{\text{adsorbate}} + E_{\text{slab}})$, where $E_{\text{adsorbate/slab}}$, $E_{\text{adsorbate}}$, and E_{slab} are the total energies of adsorbate–slab system, free adsorbate, and bare slab respectively.

Simulations for the formation mechanism of HEA NPs via H_2 spillover were performed using a $\text{TiO}_2(101)$ slab with 2×2 surface unit cell and 3-layer thickness was constructed with a vacuum thickness of 20 \AA , on which a square pyramidal Pd_5 cluster was loaded. The top-layer atoms allowed to relax during geometry optimizations and the other layers fixed at the corresponding bulk positions.

For the cohesive energy (E_c) calculation of pure metal and HEA clusters composed of Co, Ni, Cu, Ru, and Pd, the plane wave based program, Castep was employed.^{54,55} The PBE functional was used together with the ultrasoft-core potentials.⁵⁶ The basis set cutoff energy was set to 351 eV. The electron configurations of the atoms were Co: $3d^7 4s^2$, Ni: $3d^8 4s^2$, Cu: $3d^{10} 4s^1$, Ru: $4s^2 4p^6 4d^7 5s^1$, and Pd: $4d^{10}$. Sphere like 79 and 81 atom clusters were used for FCC and HCP metals, and the clusters were placed in a cubic cell with a side of 30 \AA . For the alloy cluster preparation, Pd atoms in Pd_{79} cluster were randomly replaced by Co, Ni, Cu, and Ru atoms, and $\text{Co}_{16}\text{Ni}_{15}\text{Cu}_{16}\text{Ru}_{16}\text{Pd}_{16}$ cluster was built. E_c was defined by the equation $E_c = (E_{\text{cluster}} - mE_{\text{atom}})/m$, where E_{cluster} and E_{atom} are the total energies of the pure metal or alloy cluster, and isolated single atom, respectively. m is the total number of atoms.

DFT based molecular dynamics (MD) calculations were also performed to estimate the difference in diffusion coefficients (D) between pure metal and HEA clusters employing Castep. Firstly, the structures of pure metal and HEA clusters were optimized, and then the optimized structures were subjected to MD calculations. The conditions are NVE ensemble, 900 K, time step: 1 fs, and 100 steps. D was evaluated from the mean-square displacement according to Eq.1.

$$D = \frac{1}{6} \frac{\langle |r(t_2) - r(t_1)|^2 \rangle}{t_2 - t_1} \quad (1)$$

, where t_1 and t_2 are the initial and final times of simulation interval. The D was evaluated between the start and end ($t_1 = 0$ and $t_2 = 100$) of simulation. The intermediate D values per each ten steps were also calculated to check the convergence of simulation.

Catalytic activity trials

The performance of each catalyst was evaluated using a fixed-bed reactor system in which a portion of catalyst (50 mg) was placed into a quartz cell with an internal diameter of 17 mm, held within an electric oven. The as-prepared catalyst was pretreated by heating at $5\text{ }^{\circ}\text{C}\cdot\text{min}^{-1}$ to $400\text{ }^{\circ}\text{C}$ in a flow of H_2 (20 mL/min) for 2 h. The sample was subsequently exposed to a $\text{N}_2/\text{H}_2/\text{CO}_2$ mixture having a 4/5/1 composition (total flow of $50\text{ mL}\cdot\text{min}^{-1}$, $\text{SV} = 6000\text{ mL}\cdot\text{g}^{-1}\cdot\text{h}^{-1}$). Reaction products were analysed online using a gas chromatograph (Shimadzu GC-14B) equipped with an active carbon column connected to a thermal conductivity detector followed by a flame ionization detector equipped with a methanizer.

ETEM observation

The effect of electron irradiation was monitored using an ETEM apparatus (Titan ETEM G2, Thermo Fisher Scientific Inc., USA) with a Cs-corrector of the objective lens, a monochromator and a K3-IS Direct Detection camera (Gatan, Inc., USA). The accelerating voltage and electron current flux were set at 300 kV and $2\text{ A}/\text{cm}^2$, respectively. The observation in this condition does not cause serious damage to TiO_2 support.⁵⁷ The base pressure around specimen was kept below $1\times 10^{-5}\text{ Pa}$.

Data Availability

All data generated and analysed during this study are included in this article and its Supplementary Information or are available from the corresponding authors upon reasonable request.

References

1. Yeh, J.-W., Chen, S.-K., Lin, S.-J., Gan, J.-Y., Chin, T.-S., Shun, T.-T., Tsau, C.-H. & Chang, S.-Y. Nanostructured High-Entropy Alloys with Multiple Principal Elements: Novel Alloy Design Concepts and Outcomes. *Adv. Eng. Mater.* **6**, 299–303 (2004).
2. Cantor, B., Chang, I. T. H., Knight, P. & Vincent, A. J. B. Microstructural Development in Equiatomic Multicomponent Alloys. *Mater. Sci. Eng.: A* **375–377**, 213–218 (2004).
3. Ye, Y. F., Wang, Q., Lu, J., Liu, C. T. & Yang, Y. High-Entropy Alloy: Challenges and Prospects. *Mater. Today* **19**, 349–362 (2016).
4. George, E. P., Raabe, D. & Ritchie, R. O. High-Entropy Alloys. *Nat. Rev. Mater.* **4**, 515–534 (2019).
5. Song, B., Yang, Y., Rabbani, M., Yang, T. T., He, K., Hu, X., Yuan, Y., Ghildiyal, P., Dravid, V. P., Zachariah, M. R., Saidi, W. A., Liu, Y. & Shahbazian-Yassar, R. In Situ Oxidation Studies of High-Entropy Alloy Nanoparticles. *ACS Nano* **14**, 15131–15143 (2020).
6. Otto, F., Yang, Y., Bei, H. & George, E. P. Relative Effects of Enthalpy And Entropy on The Phase Stability of Equiatomic High-Entropy Alloys. *Acta Mater.* **61**, 2628–2638 (2013).

7. Fu, Z., Chen, W., Wen, H., Zhang, D., Chen, Z., Zheng, B., Zhou, Y. & Lavernia, E. J. Microstructure and Strengthening Mechanisms in an FCC Structured Single-Phase Nanocrystalline Co₂₅Ni₂₅Fe₂₅Al_{7.5}Cu_{17.5} High-Entropy Alloy. *Acta Mater.* **107**, 59–71 (2016).
8. Brif, Y., Thomas, M. & Todd, I. The Use of High-Entropy Alloys in Additive Manufacturing. *Scr. Mater.* **99**, 93–96 (2015).
9. Fujieda, T., Shiratori, H., Kuwabara, K., Kato, T., Yamanaka, K., Koizumi, Y. & Chiba, A. First Demonstration of Promising Selective Electron Beam Melting Method for Utilizing High-Entropy Alloys as Engineering Materials. *Mater. Lett.* **159**, 12–15 (2015).
10. Xin, Y., Li, S., Qian, Y., Zhu, W., Yuan, H., Jiang, P., Guo, R. & Wang, L. High-Entropy Alloys as a Platform for Catalysis: Progress, Challenges, and Opportunities. *ACS Catal.* **10**, 11280–11306 (2020).
11. Tomboc, G. M., Kwon, T., Joo, J. & Lee, K. High Entropy Alloy Electrocatalysts: a Critical Assessment of Fabrication and Performance. *J. Mater. Chem. A* **8**, 14844–14862 (2020).
12. Yao, Y., Huang, Z., Xie, P., Lacey, S. D., Jacob, R. J., Xie, H., Chen, F., Nie, A., Pu, T., Rehwoldt, M., Yu, D., Zachariah, M. R., Wang, C., Shahbazian-Yassar, R., Li, J. & Hu, L. Carbothermal Shock Synthesis of High-Entropy-Alloy Nanoparticles. *Science* **359**, 1489–1494 (2018).
13. Xie, P., Yao, Y., Huang, Z., Liu, Z., Zhang, J., Li, T., Wang, G., Shahbazian-Yassar, R., Hu, L. & Wang, C. Highly Efficient Decomposition of Ammonia using High-Entropy Alloy Catalysts. *Nat. Commun.* **10**, 4011 (2019).
14. Yao, Y., Liu, Z., Xie, P., Huang, Z., Li, T., Morris, D., Finprock, Z., Zhou, J., Jiao, M., Gao, J., Mao, Y., Miao, J., Zhang, P., Shahbazian-Yassar, R., Wang, C., Wang, G. & Hu, L. Computationally Aided, Entropy-Driven Synthesis of Highly Efficient and Durable Multi-Elemental Alloy Catalysts. *Sci. Adv.* **6**, eaaz0510 (2020).
15. Liu, M., Zhang, Z., Okejiri, F., Yang, S., Zhou, S. & Dai, S. Entropy-Maximized Synthesis of Multimetallic Nanoparticle Catalysts via a Ultrasonication-Assisted Wet Chemistry Method under Ambient Conditions. *Adv. Mater. Interfaces* **6**, 1900015 (2019).
16. Bondesgaard, M., Broge, N. L. N., Mamakhel, A., Bremholm, M. & Iversen, B. B. General Solvothermal Synthesis Method for Complete Solubility Range Bimetallic and High-Entropy Alloy Nanocatalysts. *Adv. Funct. Mater.* **29**, 1905933 (2019).
17. Wu, D., Kusada, K., Yamamoto, T., Toriyama, T., Matsumura, S., Kawaguchi, S., Kubota, Y. & Kitagawa, H. Platinum-Group-Metal High-Entropy-Alloy Nanoparticles. *J. Am. Chem. Soc.* **142**, 13833–13838 (2020).
18. Wu, D., Kusada, K., Yamamoto, T., Toriyama, T., Matsumura, S., Gueye, I., Seo, O., Kim, J., Hiroi, S., Sakata, O., Kawaguchi, S., Kubota, Y. & Kitagawa, H. On the Electronic Structure and Hydrogen Evolution Reaction Activity of Platinum Group Metal-Based High-Entropy-Alloy Nanoparticles. *Chem. Sci.* (2020).
19. Gao, S., Hao, S., Huang, Z., Yuan, Y., Han, S., Lei, L., Zhang, X., Shahbazian-Yassar, R. & Lu, J. Synthesis of High-Entropy Alloy Nanoparticles on Supports by the Fast Moving Bed Pyrolysis. *Nat. Commun.* **11**, 2016 (2020).

20. Prins, R. Hydrogen Spillover. Facts and Fiction. *Chem. Rev.* **112**, 2714–2738 (2012).
21. Choi, M., Yook, S. & Kim, H. Hydrogen Spillover in Encapsulated Metal Catalysts: New Opportunities for Designing Advanced Hydroprocessing Catalysts. *ChemCatChem* **7**, 1048–1057 (2015).
22. Murakami, K. & Sekine, Y. Recent Progress in Use and Observation of Surface Hydrogen Migration over Metal Oxides. *Phys. Chem. Chem. Phys.* **22**, 22852–22863 (2020).
23. Chen, L., Cooper, A. C., Pez, G. P. & Cheng, H. On the Mechanisms of Hydrogen Spillover in MoO₃. *J. Phys. Chem. C* **112**, 1755–1758 (2008).
24. Sha, X., Chen, L., Cooper, A. C., Pez, G. P. & Cheng, H. Hydrogen Absorption and Diffusion in Bulk α -MoO₃. *J. Phys. Chem. C* **113**, 11399–11407 (2009).
25. Prins, R., Palfi, V. K. & Reiher, M. Hydrogen Spillover to Nonreducible Supports. *J. Phys. Chem. C* **116**, 14274–14283 (2012).
26. Karim, W., Spreafico, C., Kleibert, A., Gobrecht, J., VandeVondele, J., Ekinici, Y. & van Bokhoven, J. A. Catalyst Support Effects on Hydrogen Spillover. *Nature* **541**, 68–71 (2017).
27. Masuda, S., Shun, K., Mori, K., Kuwahara, Y. & Yamashita, H. Synthesis of a Binary Alloy Nanoparticle Catalyst with an Immiscible Combination of Rh and Cu Assisted by Hydrogen Spillover on a TiO₂ Support. *Chem. Sci.* **11**, 4194–4203 (2020).
28. Mori, K., Miyawaki, K. & Yamashita, H. Ru and Ru–Ni Nanoparticles on TiO₂ Support as Extremely Active Catalysts for Hydrogen Production from Ammonia–Borane. *ACS Catal.* **6**, 3128–3135 (2016).
29. Zhang, Y., Zhou, Y. J., Lin, J. P., Chen, G. L. & Liaw, P. K. Solid-Solution Phase Formation Rules for Multi-component Alloys. *Adv. Eng. Mater.* **10**, 534–538 (2008).
30. Zhu, H., Qin, Z., Shan, W., Shen, W. & Wang, J. Pd/CeO₂–TiO₂ Catalyst for CO Oxidation at Low Temperature: a TPR Study with H₂ and CO as Reducing Agents. *J. Catal.* **225**, 267–277 (2004).
31. Mori, K., Sano, T., Kobayashi, H. & Yamashita, H. Surface Engineering of a Supported PdAg Catalyst for Hydrogenation of CO₂ to Formic Acid: Elucidating the Active Pd Atoms in Alloy Nanoparticles. *J. Am. Chem. Soc.* **140**, 8902–8909 (2018).
32. Digne, M., Sautet, P., Raybaud, P., Euzen, P. & Toulhoat, H. Use of DFT to Achieve a Rational Understanding of Acid–Basic Properties of γ -Alumina Surfaces. *J. Catal.* **226**, 54–68 (2004).
33. Gu, J., Wang, J. & Leszczynski, J. Structure and Energetics of (111) Surface of γ -Al₂O₃: Insights from DFT Including Periodic Boundary Approach. *ACS Omega* **3**, 1881–1888 (2018).
34. Wang, W., Wang, S., Ma, X. & Gong, J. Recent Advances in Catalytic Hydrogenation of Carbon Dioxide. *Chem. Soc. Rev.* **40**, 3703–3727 (2011).
35. Kondratenko, E. V., Mul, G., Baltrusaitis, J., Larrazábal, G. O. & Pérez-Ramírez, J. Status and Perspectives of CO₂ Conversion into Fuels and Chemicals by Catalytic, Photocatalytic and Electrocatalytic Processes. *Energy Environ. Sci.* **6**, 3112–3135 (2013).
36. Kim, S. S., Lee, H. H. & Hong, S. C. A Study on the Effect of Support's Reducibility on the Reverse Water-Gas Shift Reaction over Pt Catalysts. *Appl. Catal. A* **423**, 100–107 (2012).

37. Centi, G., Quadrelli, E. A. & Perathoner, S. Catalysis for CO₂ Conversion: a Key Technology for Rapid Introduction of Renewable Energy in the Value Chain of Chemical Industries. *Energy Environ. Sci.* **6**, 1711–1731 (2013).
38. Aziz, M. A. A., Jalil, A. A., Triwahyono, S. & Ahmad, A. CO₂ Methanation over Heterogeneous Catalysts: Recent Progress and Future Prospects. *Green Chem.* **17**, 2647–2663 (2015).
39. Sreedhar, I., Varun, Y., Singh, S. A., Venugopal, A. & Reddy, B. M. Developmental Trends in CO₂ Methanation using Various Catalysts. *Catal. Sci. Tech.* **9**, 4478–4504 (2019).
40. Vogt, C., Monai, M., Kramer, G. J. & Weckhuysen, B. M. The Renaissance of the Sabatier Reaction and Its Applications on Earth and in Space. *Nat. Catal.* **2**, 188–197 (2019).
41. Li, S., Xu, Y., Chen, Y., Li, W., Lin, L., Li, M., Deng, Y., Wang, X., Ge, B., Yang, C., Yao, S., Xie, J., Li, Y., Liu, X. & Ma, D. Tuning the Selectivity of Catalytic Carbon Dioxide Hydrogenation over Iridium/Cerium Oxide Catalysts with a Strong Metal–Support Interaction. *Angew. Chem. Int. Ed.* **56**, 10761–10765 (2017).
42. Zhang, J., Deo, S., Janik, M. J. & Medlin, J. W. Control of Molecular Bonding Strength on Metal Catalysts with Organic Monolayers for CO₂ Reduction. *J. Am. Chem. Soc.* **142**, 5184–5193 (2020).
43. Li, X., Lin, J., Li, L., Huang, Y., Pan, X., Collins, S. E., Ren, Y., Su, Y., Kang, L., Liu, X., Zhou, Y., Wang, H., Wang, A., Qiao, B., Wang, X. & Zhang, T. Controlling CO₂ Hydrogenation Selectivity by Metal-Supported Electron Transfer. *Angew. Chem. Int. Ed.* **59**, 19983–19989 (2020).
44. Pedersen, J. K., Batchelor, T. A. A., Bagger, A. & Rossmeisl, J. High-Entropy Alloys as Catalysts for the CO₂ and CO Reduction Reactions. *ACS Catal.* **10**, 2169–2176 (2020).
45. Azcárate, J. C., Fonticelli, M. H. & Zelaya, E. Radiation Damage Mechanisms of Monolayer-Protected Nanoparticles via TEM Analysis. *J. Phys. Chem. C* **121**, 26108–26116 (2017).
46. Surrey, A., Pohl, D., Schultz, L. & Rellinghaus, B. Quantitative Measurement of the Surface Self-Diffusion on Au Nanoparticles by Aberration-Corrected Transmission Electron Microscopy. *Nano Lett.* **12**, 6071–6077 (2012).
47. Egerton, R. F. Beam-Induced Motion of Adatoms in the Transmission Electron Microscope. *Microsc. Microanal.* **19**, 479–486 (2013).
48. Egerton, R. F., Li, P. & Malac, M. Radiation damage in the TEM and SEM. *Micron* **35**, 399–409 (2004).
49. Bugnet, M., Overbury, S. H., Wu, Z. L. & Epicier, T. Direct Visualization and Control of Atomic Mobility at {100} Surfaces of Ceria in the Environmental Transmission Electron Microscope. *Nano Lett.* **17**, 7652–7658 (2017).
50. Lawrence, E. L., Levin, B. D. A., Miller, B. K. & Crozier, P. A. Approaches to Exploring Spatio-Temporal Surface Dynamics in Nanoparticles with In Situ Transmission Electron Microscopy. *Microsc. Microanal.* **26**, 86–94 (2019).
51. Delley, B. An All-Electron Numerical Method for Solving the Local Density Functional for Polyatomic Molecules. *J. Chem. Phys.* **92**, 508–517 (1990).

52. Delley, B. From Molecules to Solids with the DMol³ Approach. *J. Chem. Phys.* **113**, 7756–7764 (2000).
53. Perdew, J. P., Burke, K. & Ernzerhof, M. Generalized Gradient Approximation Made Simple. *Phys. Rev. Lett.* **77**, 3865–3868 (1996).
54. Payne, M. C., Teter, M. P., Allan, D. C., Arias, T. A. & Joannopoulos, J. D. Iterative minimization techniques for ab initio total-energy calculations: molecular dynamics and conjugate gradients. *Rev. Mod. Phys.* **64**, 1045–1097 (1992).
55. Milman, V., Winkler, B., White, J. A., Pickard, C. J., Payne, M. C., Akhmatkaya, E. V. & Nobes, R. H. Electronic Structure, Properties, and Phase Stability of Inorganic Crystals: A Pseudopotential Plane-Wave Study. *Inter. J. Quantum Chem.* **77**, 895–910 (2000).
56. Vanderbilt, D. Soft Self-Consistent Pseudopotentials in a Generalized Eigenvalue Formalism. *Phys. Rev. B* **41**, 7892–7895 (1990).
57. Kuwauchi, Y., Yoshida, H., Akita, T., Haruta, M. & Takeda, S. Intrinsic Catalytic Structure of Gold Nanoparticles Supported on TiO₂. *Angew. Chem. Int. Ed.* **51**, 7729–7733 (2012).
58. Zhu, B., Thrimurthulu, G., Delannoy, L., Louis, C., Mottet, C., Creuze, J., Legrand, B. & Guesmi, H. Evidence of Pd Segregation and Stabilization at Edges of AuPd Nano-Clusters in the Presence of CO: A Combined DFT and DRIFTS Study. *J. Catal.* **308**, 272–281 (2013).

Declarations

Acknowledgement

The present work was supported by the Grant-in-Aid for Scientific Research from the Ministry of Education, Culture, Sports, Science and Technology (MEXT) of Japan (no. T19K220820 and A18H020740), Element Strategy Initiative of MEXT, Japan (no. JPMXP0112101003), and “Dynamic Alliance for Open Innovation Bridging Human, Environment and Materials” from MEXT.

Author Contributions

K.M. supervised the project and wrote the manuscript. N.H performed the catalyst preparation and characterization. K.M. and H.K. performed MD calculations. N.K. and H.Y. performed the ETEM experiment. H.Y. helped supervise the project. The manuscript was written through the discussion with all authors. All authors have given approval to the final version of manuscript.

Additional Information

Supporting Information accompanies this paper.

Competing Interests: The authors declare no competing interests.

Figures

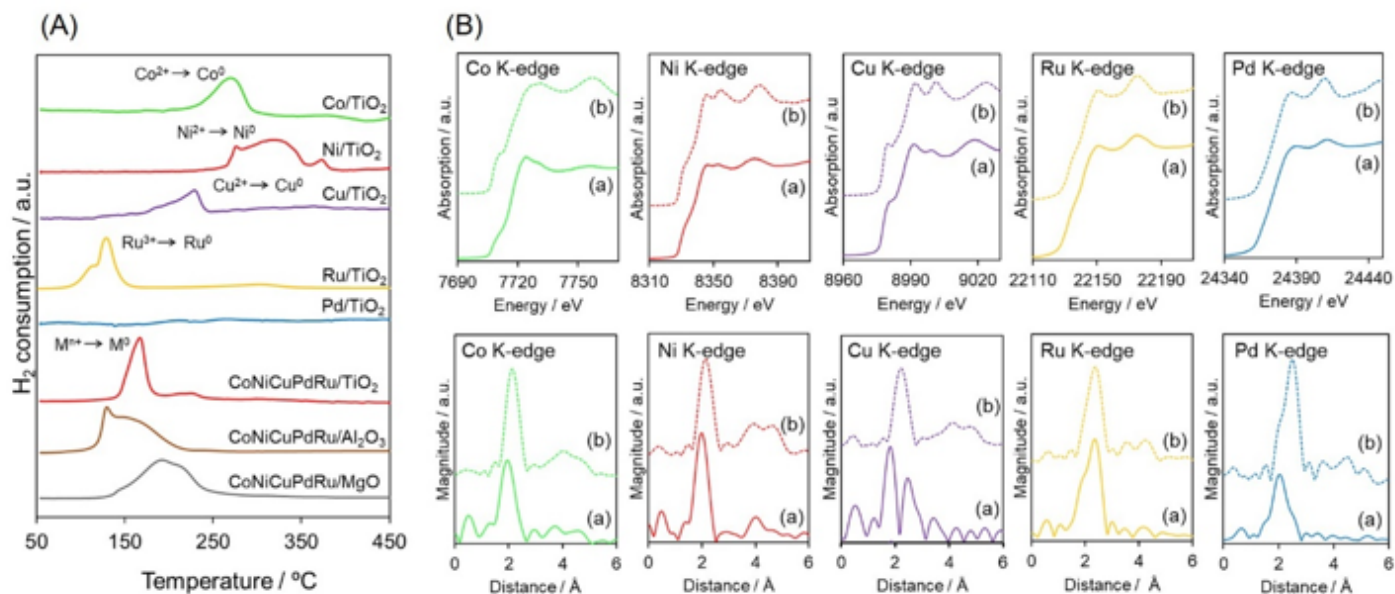


Figure 1

Characterization of the reduction sequence. (A) H₂-TPR profiles for the as-deposited mono- and quinary-component samples supported on TiO₂, Al₂O₃ and MgO. (B) In situ XANES and FT-EXAFS spectra at the Co, Ni, Cu, Ru and Pd K-edge acquired from (a) CoNiCuRuPd/TiO₂ after reduction under H₂ at 500 °C and (b) the corresponding foil reference materials.

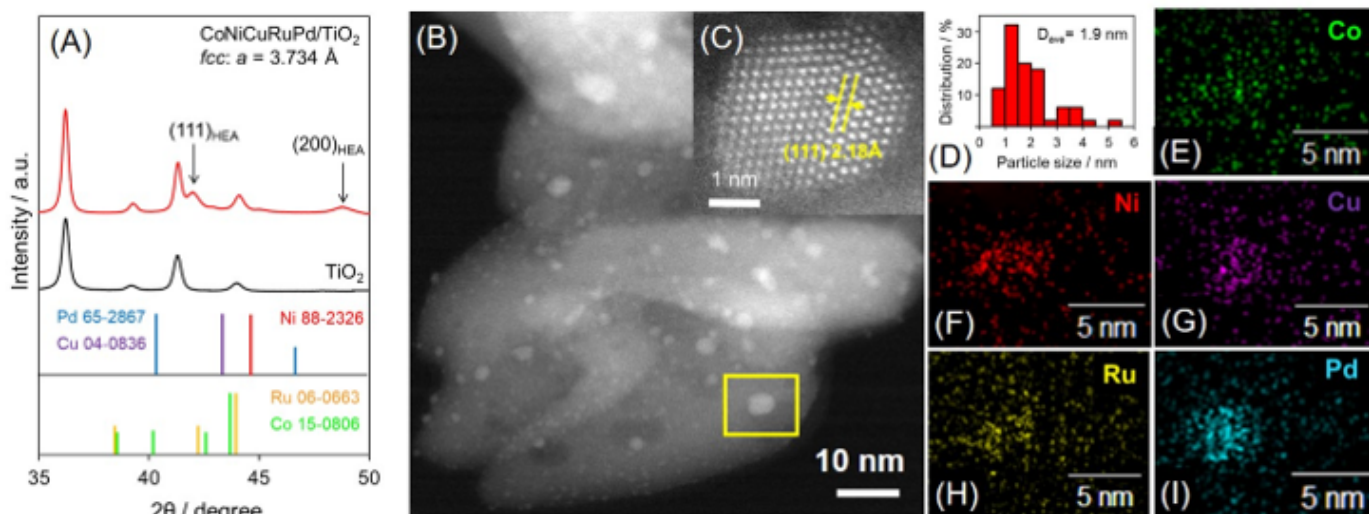


Figure 2

Characterization of CoNiCuRuPd/TiO₂. (A) XRD pattern, (B) and (C) HAADF-STEM images, (D) particle size distribution, and (E)-(I) EDX mapping of the various elements.

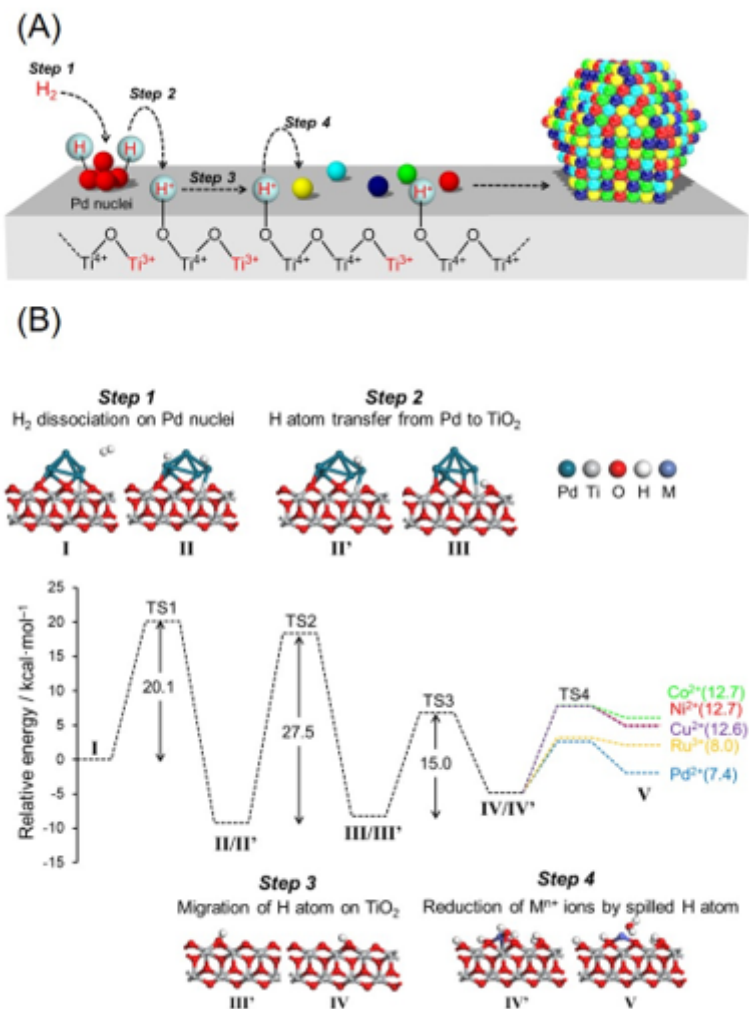


Figure 3

Formation mechanism of HEA NPs on a TiO₂ support assisted by hydrogen spillover. (A) Schematic illustration of the elementary steps and (B) the potential energy profile of processes on the TiO₂(101) as obtained from DFT calculations. The values in parentheses are the calculated energy barriers for each Mⁿ⁺ cation in step 4.

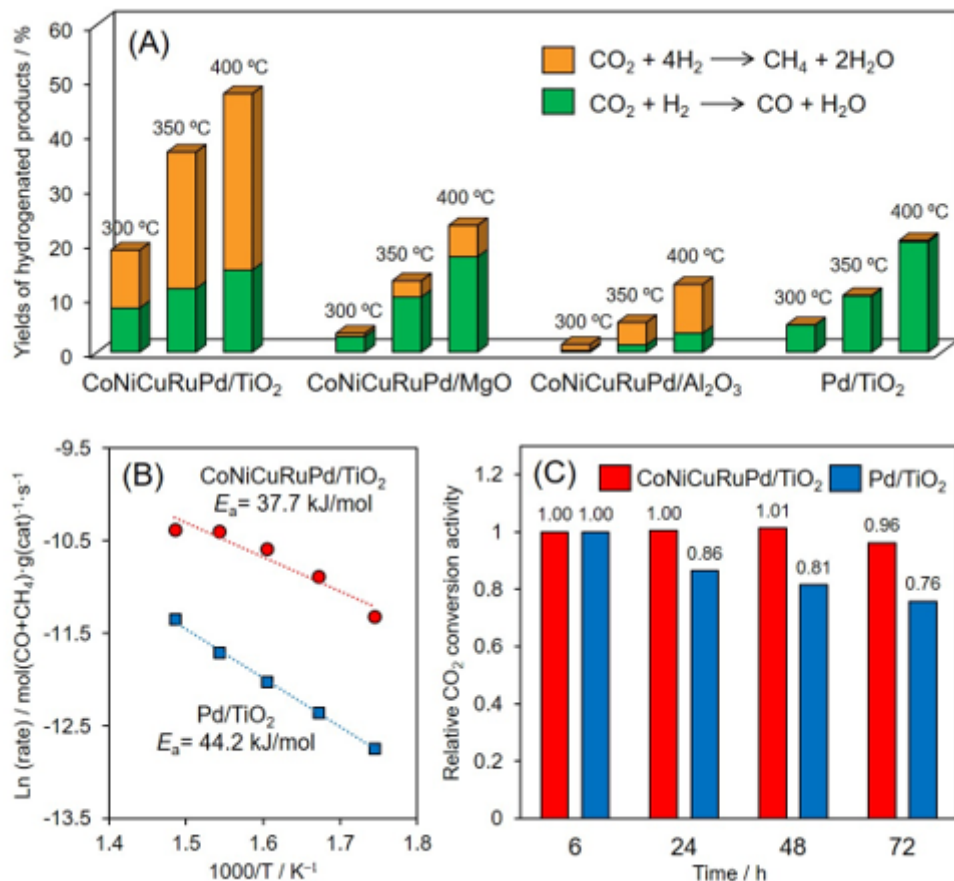


Figure 4

Comparison of catalytic activities during atmospheric pressure CO₂ hydrogenation. (A) Yields of hydrogenated products over quinary-component alloys supported on TiO₂, MgO and Al₂O₃ and over Pd/TiO₂ at various reaction temperatures, (B) Arrhenius plots obtained from CO₂ hydrogenation data over CoNiCuRuPd/TiO₂ and Pd/TiO₂, and (C) relative activities over time, showing the durability of CoNiCuRuPd/TiO₂ and Pd/TiO₂ during CO₂ hydrogenation.

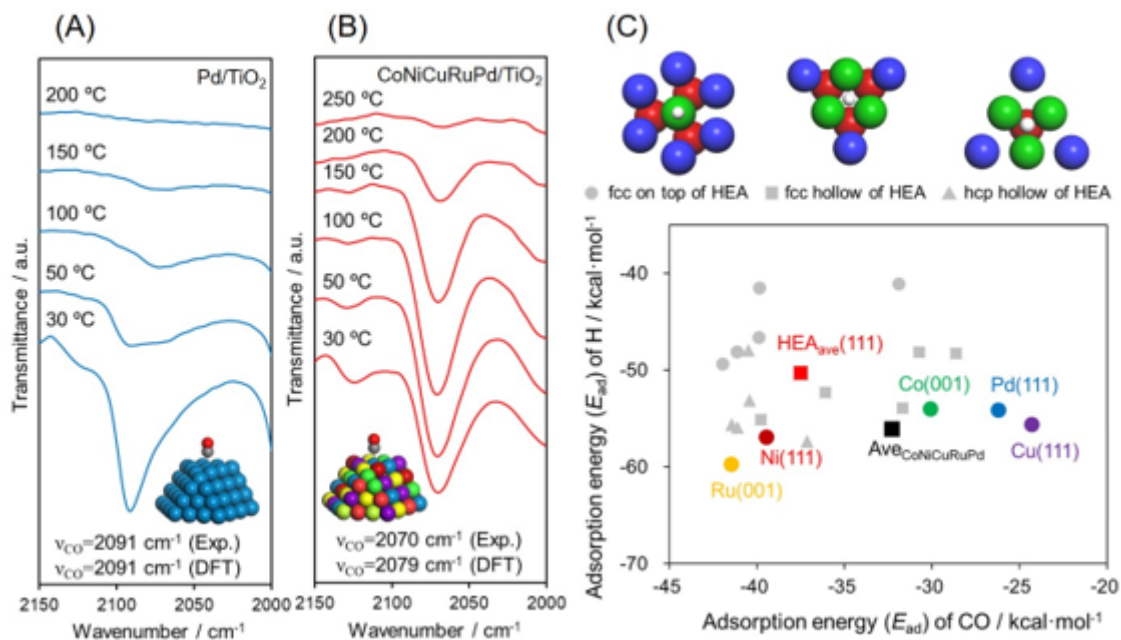


Figure 5

Comparison of adsorption characteristics. FTIR data obtained during the TPD of adsorbed CO on (A) Pd/TiO₂ and (B) CoNiCuRuPd/TiO₂. In these calculations, a correction coefficient of 1.074 was applied to adjust the vibrational frequency of CO adsorbed on the surface of an fcc Pd(111) slab model to the experimental value of 2091 cm⁻¹. (C) E_{ad} values calculated for CO and H on an upper fcc surface (●), an fcc hollow (■) and an hcp hollow (▲) for CoNiCuRuPd(111) and for pure metal slabs (Co(001), Cu(111), Ni(111), Ru(001) and Pd(111)). Here, HEA_{ave}(111) and Ave_{CoNiCuRuPd} are the averages of the E_a values for CO and H adsorption on the CoNiCuRuPd HEA and on the pure metal slabs.

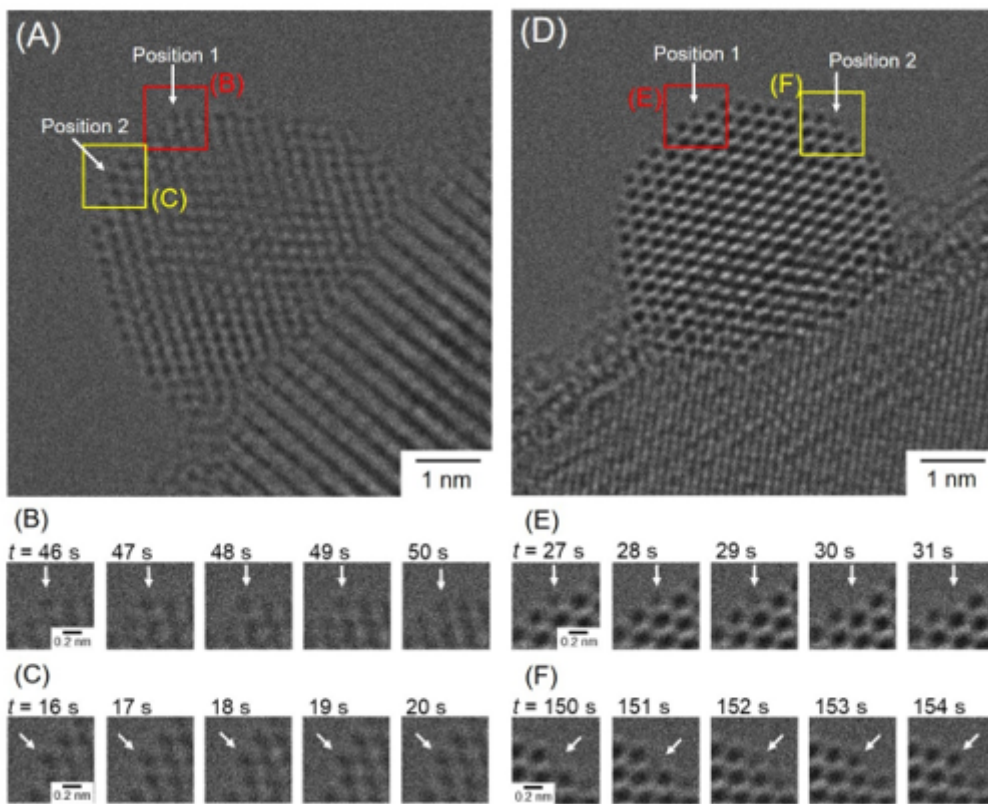


Figure 6

Stability of surface atoms under electron beam irradiation. A representative TEM image of a nanoparticle in (A) HEA/TiO₂ and (D) Pd/TiO₂, and (B)(C)(E)(F) sequential images of surface atoms taken from TEM movies (Supplementary Movies 1 and 2).

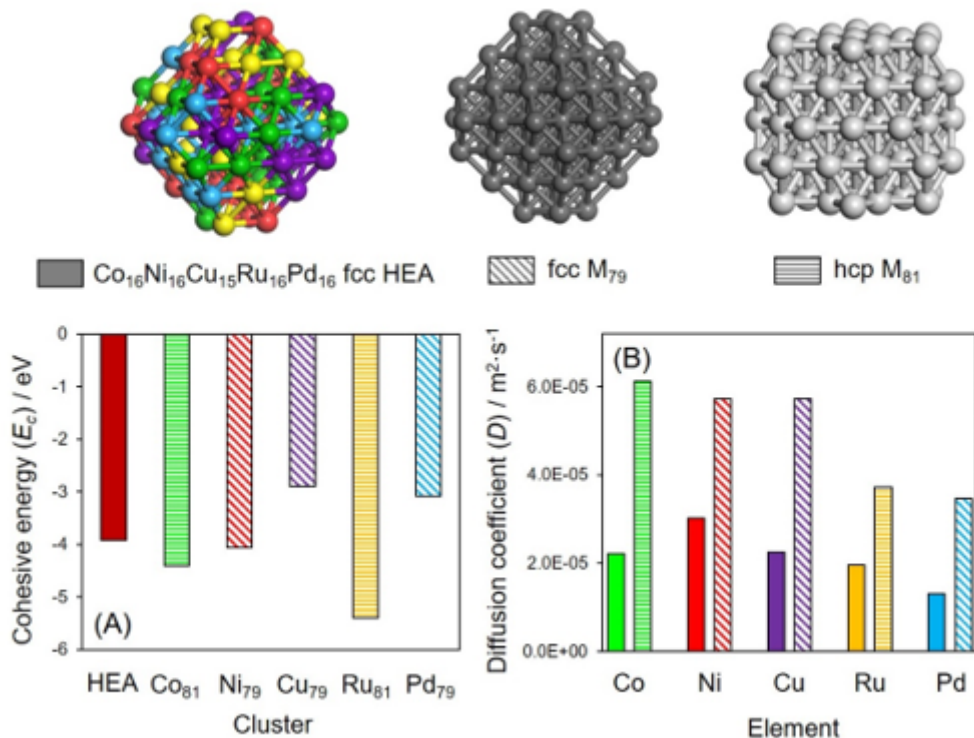


Figure 7

Sluggish diffusion in HEA NPs. (A) Cohesive energies of $\text{Co}_{16}\text{Ni}_{16}\text{Cu}_{15}\text{Ru}_{16}\text{Pd}_{16}$ HEA and M_{79} model clusters as calculated using DFT and (B) atomic diffusion coefficients for the elements in the $\text{Co}_{16}\text{Ni}_{16}\text{Cu}_{15}\text{Ru}_{16}\text{Pd}_{16}$ HEA and M_{79} models as determined by MD simulations.

Supplementary Files

This is a list of supplementary files associated with this preprint. Click to download.

- [Supplementaryinformation.pdf](#)
- [SupplementaryMovie2PdTiO2.avi](#)
- [SupplementaryMovie1HEATiO2.avi](#)